Possible high-potential ilmenite type Na_1MO_3 (M = V–Ni) cathodes realized by dominant oxygen redox reaction

M. H. N. Assadi,[1] Masashi Okubo,[2,3] Atsuo Yamada,[2,3] and Yoshitaka Tateyama[1,3,*]

[1]*Center for Green Research on Energy and Environmental Materials (GREEN), International Center for Materials Nanoarchitectonics (MANA) and Center for Materials Research by Information Integration (CMI2), National Institute for Materials Science (NIMS), 1-1 Namiki, Tsukuba, Ibaraki 305-0044, Japan*

[2]*Department of Chemical System Engineering, The University of Tokyo, 7-3-1 Hongo, Bunkyo-ku, Tokyo 113–8656, Japan*

[3]*Elements Strategy Initiative for Catalysts & Batteries (ESICB), Kyoto University, 1-30 Goryo-Ohara, Nishikyo-ku, Kyoto 615-8245, Japan*

(Received 7 March 2019; published 2 January 2020)

Identifying high-voltage cathode materials is critically important for increasing the energy density of Na ion batteries. Through a comprehensive density-functional survey, we demonstrate that oxygen redox in $R\bar{3}$ (ilmenite structure) Na_1MO_3 generates high operating voltage upon extraction and insertion of a Na ion. In the $R\bar{3}$ structure, O ions are undercoordinated by two M and two Na ions and two vacant sites, creating unhybridized O $2p$ states with a nonbonding character that are lifted closer to the Fermi level. Since O $2p$ and M t_{2g} states do not significantly overlap at the top of the valence band, the redox reaction is mainly borne on O ions. We also show that, in general, higher covalent bonding between the transition metal and oxygen results in higher voltage in this class of materials in which O redox is dominant. Furthermore, a thorough examination of the phase stability of $R\bar{3}$ Na_1MO_3 compounds reveals that Na_1VO_3 is an economical high-voltage (5.907 V) cathode with robust cyclability for Na ion batteries. Finally, although the crystal overlap Hamilton population does not indicate any significant bonding between oxidized O ions upon desodiation in Na_xMO_3 compounds, we predict that gaseous O_2 may still develop through thermodynamic decomposition of Na_1MO_3 to Na_1MO_2 in some compounds.

DOI: 10.1103/PhysRevMaterials.4.015401

I. INTRODUCTION

Many stationary and portable energy storage applications require rechargeable batteries with high-energy density [1,2]. In addition to storing high wattage, these batteries should also be made of abundant and nontoxic elements to fulfill safety and environmental expectations [3]. The latter condition has motivated intensive research efforts into Na ion batteries as a more economical alternative to the conventional Li ion variety [4–6]. However, the capacity of Na ion batteries must be improved to become comparable to that of Li ion batteries either by increasing the output voltage or the capacity before wide-scale market deployment [7,8]. One particular factor that plays a significant role in determining the energy density of a battery is the operating voltage of the cathode material. In conventional cathodes based on alkali- and transition-metal (M) oxides, in which the M ions are the sole electrochemically active elements, the redox potential of the M ion in any given compound mainly determines the voltage [9,10].

In a recent experiment, Na_xRuO_3 ($0.5 < x < 2$) was found to have a cathode capacity of 180 mA hg^{-1}, which corresponds to the extraction of ∼1.4 electrons per formula unit [11]. In this compound, the extra capacity of ∼0.4 electron is mostly compensated for by a reversible oxygen redox mechanism after the compound desodiated to Na_1RuO_3, which is of ilmenite $R\bar{3}$ crystal structure [12]. Interestingly, after the oxygen redox mechanism is triggered, $Na_{1-x}RuO_3$ experiences a voltage step from 2.2 to 3.4 V. Furthermore, the desodiation from Na_1RuO_3 to $Na_{0.5}RuO_3$ produced a flat voltage profile indicating the absence of intermediate phases. The observation of the voltage hike hints at the fact that O redox may generate higher potential than the exclusive M redox. Furthermore, recently compounds containing highly oxidized $3d$ M ions such as V^{5+}, Cr^{4+}, Mn^{5+}, and Fe^{4+} have been successfully synthesized [13–18]. These observations together offer a new possibility of raising the cathode voltage by triggering O redox in high-valent $3d$ oxides as a mean to increase the energy density of Na ion batteries. Stimulated by these experiments and by the observation of high potential associated with O redox in d^0 transition-metal oxides such as Na_xNbO_3 [12], we theoretically investigate the oxygen redox mechanisms in a range of the ilmenite-type $R\bar{3}$ Na_1MO_3 compounds in which M = V, Cr, Mn, Fe, Co, and Ni. The sodiated compounds are set to be isomorphic to $R\bar{3}$ Na_1RuO_3 in which O redox generates higher electric potential while the desodiated compounds are set to be isomorphic to the desodiated $P\bar{3}1m$ $Na_{0.5}RuO_3$ [11]. The study presented here will also establish the relationship between M−O bond ionicity and the cathode voltage when O redox is dominant, and it will determine the indicators of O_2 evolution during cycling that leads to cathode degradation [19].

II. METHODS AND MODELING SETTINGS

The $3d$ transition-metal oxides usually have strong electronic correlation effects and exhibit a variety of spin states that affect structural stability. Thus, we have carried out

*Corresponding author: TATEYAMA.Yoshitaka@nims.go.jp

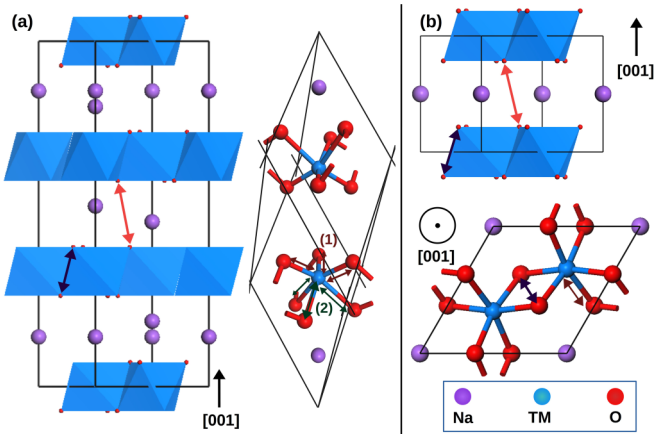

FIG. 1. The structures of ilmenite type ($R\bar{3}$) Na_1MO_3 and hexagonal ($P\bar{3}1m$) $Na_{0.5}MO_3$ in both polyhedral and ball-and-stick models are presented in (a) and (b), respectively. The ball-and-stick model of $R\bar{3}$ Na_1MO_3 represents the primitive cell. The shortest O–O distance within a polyhedron is marked with dark blue arrows, while the distance between O ions across the MO_3 planes is marked with orange arrows. Due to puckering distortion in the $R\bar{3}$ structure, there are two distinct $M-$O bond lengths. Shorter $M-$O bonds (1) are marked with brown arrows while the longer $M-$O bonds (2) are marked with green arrows.

spin-polarized density-functional theory (DFT) calculations within the projected augmented-wave (PAW) potential formalism [20] as implemented in VASP code [21,22] while the electronic populations were analyzed using LOBSTER code [23]. Brillouin zone sampling was carried out using a mesh generated by a $7 \times 7 \times 7$ Monkhorst-Pack grid for the rhombohedral and hexagonal structures, respectively, creating a spacing of ~ 0.03 Å^{-1} among k-points. The energy cutoff was set to 550 eV. To account for the $3d$ electrons' strong localization effects, we used an HSE06 hybrid exchange-correlation functional with 0.2 mixing parameter [24,25]. All structures were fully relaxed to forces smaller than 0.01 Å/eV. We also examined the magnetic stability of the compounds by comparing the energy of the ferromagnetic (FM) solution to that of the antiferromagnetic (AFM) solution ($\Delta E = E_{\mathrm{AFM}} - E_{\mathrm{FM}}$). Positive ΔE indicates a ferromagnetic ground state. The orbital-resolved electronic states and populations were approximated using the default Wigner-Seitz radii supplied with the PAW pseudopotentials.

Here, we focus on Na_xMO_3 ($M = 3d$ transition metal) with the ilmenite-type $R\bar{3}$ structure (space group 158), of which the primitive cell contains two formula units as shown in Fig. 1(a). For desodiated compounds, a primitive $P\bar{3}1m$ $Na_{0.5}MO_3$ unit cell, presented in Fig. 1(b), was used for the calculations. The $Na_{0.5}MO_3$ compound adopts the primitive hexagonal structure with space group 162 in which O is coordinated by two M ions and one Na ion.

To explore the electrochemical activity of the Na_xMO_3 cathode, we calculated the average voltage using the following equation:

$$V = \frac{[E^t(\mathrm{Na_1MO_3}) - E^t(\mathrm{Na_{0.5}MO_3}) - E^t(\mathrm{Na})]}{-0.5e} \quad (1)$$

in which $E^t(\mathrm{Na}_x\mathrm{MO}_3)$ is the total energy of the Na_xMO_3 compound, $E^t(\mathrm{Na})$ is the total energy of the elemental solid Na per atom, and e is the electron's charge.

The ionicity of the $M-$O bonds was examined by calculating the electronic localization function (ELF) for which maximum values ($\mathrm{ELF_{max}}$) are presented in Table I for Na_1MO_3 compounds and in Table II for $Na_{0.5}MO_3$ compounds. The ELF is defined as the probability density of finding a second spinlike electron at a given position if another electron is located with certainty at the same position [26]. The ELF offers a straightforward topological analysis of bonding character [27]. $\mathrm{ELF_{max}}$ approaching 1 and peaking near the anionic centers indicates higher ionicity, while $\mathrm{ELF_{max}}$ localized on the bond centers indicates covalence bonding. For instance, in highly ionic NaCl, $\mathrm{ELF_{max}}$ is $\sim$0.9 and peaks near the Cl centers. The ELF isosurfaces of all compounds are presented in Fig. S3 in the Supplemental Material [28]. Bonding tendencies and strengths were determined by analyzing the crystal orbital Hamilton population (COHP), which is calculated by weighing the density of states by the overlap elements of the Hamiltonian, partitioning the band-structure energy into bonding, nonbonding, and antibonding contributions. Positive $-$COHP values indicate bonding interaction, while negative $-$COHP values indicate antibonding interaction, respectively. The integrated $-$COHP curves result in an energy value that can be interpreted as bonding strength [29].

III. RESULTS AND DISCUSSIONS

The calculated electronic properties of the $R\bar{3}$ Na_1MO_3 and $P\bar{3}1m$ $Na_{0.5}MO_3$ compounds are presented in Tables I

TABLE I. The nominal and calculated $3d$ shell electronic population, the energy difference between ferromagnetic and antiferromagnetic states (ΔE), the maximum value of the electronic localization function (ELF), and the $M-$O bond lengths are given for $R\bar{3}$ Na_1MO_3 compounds.

System	Projected M spin population (e) (Na_1MO_3)	Corresponding electronic configuration (Na_1MO_3)	ΔE (meV)	$\mathrm{ELF_{max}}$	$(M\text{–O})_1$ (Å)	$(M\text{–O})_2$ (Å)
Na_1VO_3	0.000	$t_{2g}^0 e_g^0$	None	0.601	1.726	2.069
Na_1CrO_3	0.990	$t_{2g}^1 e_g^0$	84.814	0.678	1.804	1.875
Na_1MnO_3	1.966	$t_{2g}^2 e_g^0$	192.896	0.657	1.827	1.857
Na_1FeO_3	2.777	$t_{2g}^3 e_g^0$	-188.433	0.626	1.819	1.849
Na_1CoO_3	1.644	$t_{2g}^4 e_g^0$	-23.976	0.633	1.812	1.822
Na_1NiO_3	0.891	$t_{2g}^5 e_g^0$	-202.042	0.680	1.845	1.847

TABLE II. The nominal and calculated $3d$ shell electronic population, the energy difference between ferromagnetic and antiferromagnetic states (ΔE), the maximum value of the electronic localization function, and the $M-$O bond length are given for $P\bar{3}1m$ $Na_{0.5}MO_3$ compounds.

Compound	Projected M spin population (e) (Na_1MO_3)	Corresponding electronic configuration (Na_1MO_3)	ΔE (meV)	ELF_{max}	$M-$O (Å)
$Na_{0.5}VO_3$	0.043	$t_{2g}^0 e_g^0$	230.124	0.564	1.852
$Na_{0.5}CrO_3$	1.000	$t_{2g}^1 e_g^0$	576.533	0.518	1.828
$Na_{0.5}MnO_3$	1.950	$t_{2g}^2 e_g^0$	654.099	0.512	1.855
$Na_{0.5}FeO_3$	2.769	$t_{2g}^3 e_g^0$	406.551	0.530	1.818
$Na_{0.5}CoO_3$	1.534	$t_{2g}^4 e_g^0$	648.618	0.541	1.808
$Na_{0.5}NiO_3$	0.899	$t_{2g}^5 e_g^0$	402.252	0.540	1.833

and II, respectively, while their relevant lattice parameters can be found in Tables S1 and S2 in the Supplemental Material [28]. Site-projected magnetic moments, presented in Table I, show that all M ions are stabilized in the low spin state. Furthermore, Cr, Mn, and Ni are in the nearly perfect oxidation state of +5 indicating an overall ionic character of the $M-$O bonds in the corresponding Na_1MO_3 compounds. The local magnetic moment for the M ions in Na_1FeO_3 and Na_1CoO_3, however, is smaller than the values expected for the +5 oxidation state by $0.231e$ and $0.466e$, respectively, indicating a slight deviance from ionicity toward covalency. In the case of Na_1VO_3, although the spin of V indicates that the V ion is fully ionized, the V–O bond covalency might be driven by a larger bond charge population.

The ELF_{max} values also reflect an ionicity trend similar to the prediction of the calculated spin populations. Since no compound has an ELF_{max} value smaller than 0.601, all Na_1MO_3 compounds are inferred, with varying degrees, to have ionic character. More specifically, the ionicity of the $M-$O bond is comparatively weaker in Na_1VO_3, Na_1FeO_3, and Na_1CoO_3 as their ELF_{max} values are smaller than their neighboring compounds. Structurally, the MO_6 octahedra in $R\bar{3}$ structures generally undergo puckering distortion, which creates two $M-$O bond lengths, marked (1) and (2) in Fig. 1(a). The puckering distortion splits the t_{2g} orbitals into a set of doubly occupied low-lying e_g^π orbitals and a singly occupied high-lying a_{1g} state. In Na_1CrO_3 and Na_1MnO_3, this splitting is clearly observed. According to the values presented in Table I, however, the puckering distortion tapers off as the atomic number of the M ion increases, and the length difference between the short and long bonds decreases, reducing the puckering-induced splitting to a negligible effect.

Upon desodiation and therefore transitioning to the $P\bar{3}1m$ $Na_{0.5}MO_3$ phase, M ions mostly retain their electronic population, as demonstrated by the meagre change in the spin population localized on the M ions presented in Table III. Moreover, the $Na_{0.5}MO_3$ compounds are, in general, less ionic than the Na_1MO_3 compounds as their ELF_{max} is slightly smaller than that of their Na_1MO_3 counterparts and approaches 0.5. The weaker ionic bonding in $Na_{0.5}MO_3$ compounds is also implied from the shorter $M-$O bonds, which promote greater hybridization between O $2p$ and M $3d$ states; the $M-$O bonds in the $Na_{0.5}MO_3$ compounds are on average ∼0.014 Å shorter than those in the Na_1MO_3 compounds.

As shown in Table III, during the desodiation process, the total charge associated with the M ions does not significantly change. On the other hand, the total charge associated with the O ions decreases by an average of $\sim 1.34\,e$/O for all compounds, indicating that these are O ions that primarily compensate for the extracted electron that accompanies the vacating Na atom. The portion of the single hole created by Na atom extraction that is localized on O sites is 80.28% for Na_xVO_3, 87.97% for Na_xCrO_3, 92.38% for Na_xMnO_3, 89.91% for Na_xFeO_3, 110.52% for Na_xCoO_3, and 85.65% for Na_xNiO_3. The peculiar case of having more than one hole on O sites in Na_xCoO_3 originates from the fact that the Co ions are partly reduced by $0.11\,e$/Co upon desodiation. Consequently, the extra holes on the oxygen sites were created to maintain charge neutrality.

Charge compensation by O in Na_xMO_3 compounds can be attributed to the electronic structure of these compounds. As shown in Fig. 2, in all Na_1MO_3 compounds, O $2p$ states are dominant near the valence-band maximum region while the M $3d$ states mostly gravitate toward the middle and the bottom of the valence band. O dominance near the valence-band

TABLE III. The net change in the Bader electronic population of M $3d$ and O $2p$ shells upon desodiation in Na_xMO_3 compounds, the calculated voltage, and the shortest O–O distances for both Na_1MO_3 and $Na_{0.5}MO_3$ compounds.

Compound	M population change (e)	O population change (e)	Voltage (V)	O–O distance (Å) (Na_1MO_3)	O–O distance (Å) ($Na_{0.5}MO_3$)
Na_xVO_3	−0.043	−0.134	5.907	2.401	2.368
Na_xCrO_3	−0.010	−0.147	4.239	2.283	2.342
Na_xMnO_3	0.016	−0.154	4.530	2.347	2.427
Na_xFeO_3	0.008	−0.150	5.178	2.324	2.381
Na_xCoO_3	0.110	−0.184	3.493	2.291	2.368
Na_xNiO_3	−0.008	−0.143	3.979	2.401	2.386

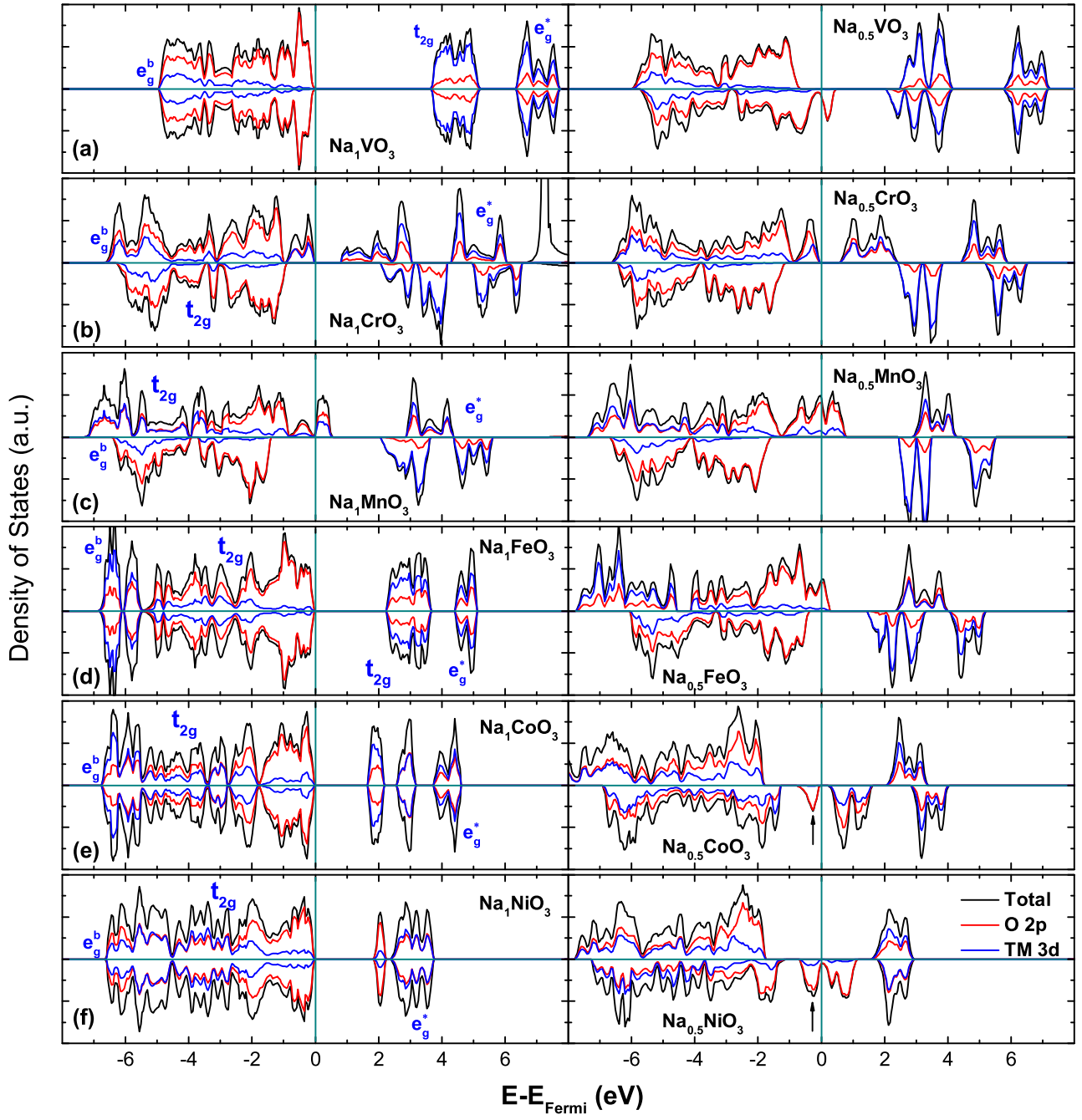

FIG. 2. The density of states of Na_1MO_3 and $Na_{0.5}MO_3$ are represented in the first and second columns, respectively. The black, red, and blue lines correspond to the total, O 2p and M 3d states, respectively.

maximum is particularly more prominent in antiferromagnetic Na_1FeO_3, Na_1CoO_3, and Na_1NiO_3 and nonmagnetic Na_1VO_3. This is because spin-up and spin-down channels are degenerate and consequently both are equally present at the valence-band maximum. In ferromagnetic Na_1CrO_3 and Na_1MnO_3, however, due to the magnetic exchange splitting [9], the spin-down channel is relegated to lower energies and, as a result, the top of the valence band is primarily comprised of O 2p states from the spin-up channel with little contribution from the spin-down channel. The general features of the electronic structure of the Na_1MO_3 compounds are markedly different from the Na_1MO_2 compounds in which M 3d states dominate the valence-band maximum region [30,31]. In desodiated $Na_{0.5}MO_3$ compounds, M 3d states still mostly reside in the bottom of the valence band, again indicating the minimal participation of 3d electrons in the redox reaction. Moreover, as in the right-hand side panels of Fig. 2, in $Na_{0.5}VO_3$, $Na_{0.5}MnO_3$, $Na_{0.5}FeO_3$, and $Na_{0.5}NiO_3$ the Fermi level crosses the O states that have been partially emptied during the desodiation process, creating metallic conduction in those compounds.

The potential of Na extraction, presented in Table III, exceeds 5 V in Na_xVO_3 and Na_xFeO_3 while it exceeds 4 V in Na_xMnO_3 and Na_xCrO_3. These values are significantly higher

than those generated by the M redox in common layered rock-salt Na_1MO_2 compounds. The cathode potential in Na_xMO_2 compounds usually averages around 2.5 V [32,33] and seldom peaks at ∼4 V [34]. For instance, the cathode potential is ∼1.8 V for $NaVO_2$ [35] and ∼3.4 V for $NaFeO_2$ [36,37], significantly smaller than the voltage of Na_xVO_3 and Na_xFeO_3 predicted here. Given that M $3d$ electrons do not participate substantially in the redox reaction in Na_1MO_3 compounds, the higher potential must be attributed to the O's participation in the redox reaction. Earlier electrochemical measurements for $Li_{1.3}Nb_xM_yO_2$ compounds in which M = Mn, Fe, Co, and Ni had indeed demonstrated that the cathode potential approached ∼5 V when the O redox became dominant [38]. Moreover, we found no clear correlation between the Na extraction potential of a given Na_xMO_3 compound and the structural characteristics such as the M−O bond lengths or O−M−O bond angles, which are presented in Table S6. This lack of a clear correlation demonstrates the complex interplay between the structural and electronic factors that determine the operating potential in these compounds [39].

A close examination of the density of states in Fig. 2 reveals that in Na_1MO_3 compounds the band structure is made of one low-lying e_g^b band arising from bonding M−O hybridization and one high-lying e_g^* band originating from antibonding M−O hybridization. There is a little hybridization between M t_{2g} states and O $2p$ states in the middle of the valence band ($-4\,\text{eV} < E < -1\,\text{eV}$), which results in a general but varying tendency toward ionicity reflected in the ELF_{max} values presented in Table II. This hybridization is relatively stronger in Na_1VO_3 and Na_1FeO_3, as is evident from the sizeable spatial span of ELF_{max} around O ions in Fig. S3 in the Supplemental Material. The top of the valence band ($-2\,\text{eV} < E < 0\,\text{eV}$) is nonetheless mostly occupied with O $2p$ nonbonding states. These nonbonding $2p$ states originate from O's undercoordination in the $\bar{R}3$ structure in which each O is only coordinated with two M and two Na ions and two vacant sites. Consequently, those $2p$ orbitals along a □–O–□ configuration (□ stands for a vacant site) remain mostly unhybridized, and as a result they form states with dominantly nonbonding character that occupy the top of the valence band in all Na_1MO_3 compounds. These mostly nonbonding O $2p$ states become electrochemically labile for the redox reaction due to their position at the top of the valence band.

The voltages of different Na_xMO_3 compounds can be inversely correlated to the ionicity of the M−O bonds, i.e., the decrease in the ionicity of the M−O bond in Na_1VO_3 and Na_1FeO_3 results in higher voltage. That is because a less ionic, i.e., more covalent, M−O bond will introduce quantum-mechanical repulsion between the bonding e_g^b states and the antibonding e_g^* states, lowering the position of the valence-band top with respect to the Na/Na^+ energy level, and therefore raising the potential required for the removal of one electron. This same repulsion nonetheless decreases the voltage when the M's antibonding e_g states are occupied and constitutes the redox centers [39]. The inverse relationship between voltage and ELF_{max} holds for all compounds except for Na_xCoO_3. In the exceptional case of Na_xCoO_3, the oxygen hole states constitute a detached band in the desodiated $Na_{0.5}CoO_3$, marked with an arrow in Fig. 2(e), above the main valence band. The lack of hybridization between oxygen hole states and the main valence band decreases the stability of the $Na_{0.5}CoO_3$ compound, which in turn lowers the voltage [9]. The same effect also occurs in $Na_{0.5}NiO_3$, which has the second lowest potential.

A pressing question for O redox materials is whether gaseous O_2 molecules evolve during the redox or not. O_2 evolution can be triggered by the bonding of O_2^{n-} species at potentials higher than ∼4 V. We examine the possibility of O_2 formation through this mechanism by monitoring two indicators: the change in the −COHP of the closest neighboring O atoms, and the change in the distance between those two O atoms during the desodiation process in Na_xMO_3. Figure 3 presents the partial −COHP (−pCOHP) curves of the closest O neighbors in both Na_1MO_3 and $Na_{0.5}MO_3$ compounds as marked by dark blue arrows in Fig. 1. Noticeably, in both sodiated and desodiated compounds, antibonding −COHP states dominate the energy range near the Fermi level. Furthermore, the integrated partial −COHP (−IpCOHP) are at least an order of magnitude smaller than that of the O_2 molecule, which is calculated to be 4.421 eV and indicates a very weak O–O interaction within the Na_xMO_3 crystal framework. For Na_xVO_3 and Na_xCrO_3, the O–O interaction in both sodiated and desodiated compounds remains antibonding, indicating a lack of tendency toward the bonding of O_2^{n-} species. For Na_xFeO_3, Na_xCoO_3, and Na_xNiO_3, although the O–O interaction in the sodiated compound is weakly bonding, this interaction significantly fades away in the desodiated compounds. Only in Na_xMnO_3 does the antibonding O–O interaction in the sodiated compound change to a very weak bonding interaction in the desodiated compound.

As shown in Table III, in both $R\bar{3}$ Na_1MO_3 and $P\bar{3}1m$ $Na_{0.5}MO_3$, the shortest O–O distance that occurs within a single MO_6 octahedron is never smaller than ∼2.29 Å. In Na_xCrO_3, Na_xMnO_3, Na_xFeO_3, and Na_xCoO_3, the O–O distance even increases upon desodiation. The greater separation of O ions in Na_xMO_3 compounds originates from the non-close-packed nature of the $R\bar{3}$ crystal structure [40], as in Na_1MO_3 an O ion is coordinated by two Na and two M ions. Furthermore, in Na_xMO_3 compounds, there are three O ions for every M ion, which is in contrast to Na_xMO_2 compounds that have two O ions for each M ion. Due to this structural feature, the partial holes borne on each O ion created by the desodiation process are smaller (one-sixth of a hole per O in $Na_{0.5}MO_3$ versus one-fourth of a hole per O in Na_xMO_2), which leads to smaller O oxidation per Na extraction. The proximity of O ions across MO_6 layers, marked with orange arrows in Fig. 1, has also been identified to trigger irreversible O_2 evolution in some compounds [41,42]. As seen in Table S6, this distance in both $R\bar{3}$ Na_1MO_3 and $P\bar{3}1m$ $Na_{0.5}MO_3$ is maintained at ∼3 Å and is very unlikely to promote O–O bonding in Na_xMO_3 compounds through the bonding of oxidized O ions. Furthermore, it has been speculated that O_2 evolution during O redox can be triggered by reductive M−O coupling in which electrons are transferred from O $2p$ states into the M $3d$ states. In this scenario, such charge-spilling, which is assumed to be prominent in highly covalent M−O bonds, promotes the irreversible formation of superoxide and eventual O_2 evolution [38]. In our study, among all compounds, we only detected a minor reductive

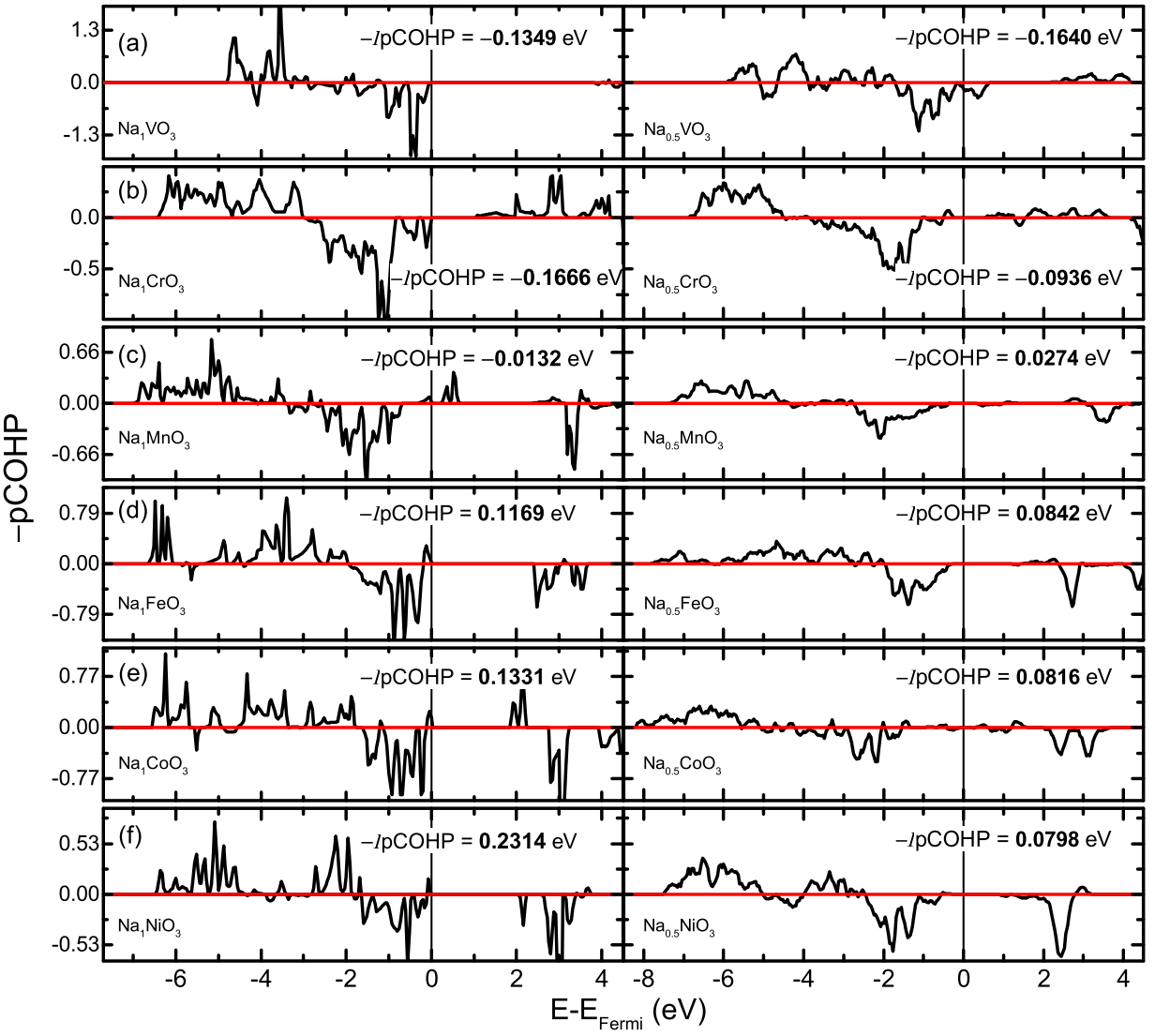

FIG. 3. The partial crystal Hamilton population overlap (−pCOHP) analysis of the closest O ions in the $R\bar{3}$ Na_1MO_3 compounds in the left column and $Na_{0.5}MO_3$ compounds in the right column as a function of energy. −IpCOHP is the integrated −pCOHP over the valence-band range. Positive and negative −pCOHP values indicate bonding and antibonding interactions.

coupling in a Co–O bond with a charge-spilling of 0.11 e/Co in Na_xCoO_3. This compound is, however, more ionic than the other compounds in which O to M charge-spilling is either absent or negligible. Given the small magnitude of this charge-spilling in Na_xCoO_3, nonetheless, we do not anticipate that it triggers the bonding of O_2^{n-} species as a more substantial charge spilling of $\sim 1e$ is required for O_2 evolution [43].

O_2 evolution can also occur due to the thermodynamic decomposition of the cathode materials where M is reduced to a more stable lower oxidation state. We examined such a possibility by calculating the decomposition enthalpy of Na_1MO_3 to Na_1MO_2 and ½O_2, as presented in Table S4. We found that among all Na_1MO_3 compounds, only Na_1VO_3 was readily stable against such decomposition. Consequently, Na_xVO_3 emerges as a candidate cathode material with the highest potential of 5.907 V that is also stable against decomposition into Na_1MO_2 and offers stable cyclability as indicated by negative O–O −IpCOHP values through Na extraction and insertion. However, for $R\bar{3}$ Na_1VO_3 to be immediately suitable for practical application, it also needs to be stable against all other competing $Na_xV_yO_z$ phases. We positively verified this criterion by examining the stability of Na_xVO_3 against all major competing phases, as presented in Table S6 in the Supplemental Material. The rest of the $R\bar{3}$ Na_1MO_3 compounds, however, do not have the lowest formation enthalpy when compared to $R\bar{3}m$ Na_1MO_2 compounds but nonetheless may still be utilized as metastable cathode materials in a similar manner to the metastable Li_2VO_3 and $Li_xV_2O_5$ compounds when they are stabilized by high-energy ball-milling [44,45].

O redox has been reported in Li excess [46,47] and cation-disorder materials [38,48]. In these classes of materials, the participation of O in redox is promoted by those O ions that are coordinated by more than three alkali-metal ions. Note that in compounds in which O is coordinated by only three alkali-metal ions, the redox reaction is compensated for by M t_{2g} or

e_g states [30]. When O ions are coordinated by more than three Li ions, some of the O $2p$ states in the Li–O–Li configuration remain unhybridized, and if their energy level is higher than the nonbonding M t_{2g} states, O redox occurs [49]. However, in $R\bar{3}$ Na_1MO_3 compounds, due to M's high oxidation state of +5, e_g states are always empty. Moreover, the occupied M t_{2g} states always adopt a nonbonding character and lie below O $2p$ nonbonding states and never dominate the top of the valence band. Given the fact that these unhybridized $2p$ states outcompete the t_{2g} states for a spot at the top of the valence band in the $R\bar{3}$ Na_1MO_3 compounds, they also dominate the charge compensation mechanism during the redox reaction. This mechanism, to some degree, resembles the redox mechanism in highly desodiated Na_2RuO_3 [11,12] and Na_2IrO_3 [50] compounds where O and M redox reactions occur simultaneously. However, due to the stronger localization effects of the $3d$ electrons, the O redox in $3d$ containing Na_1MO_3 is significantly more substantial.

In a recent electrochemical measurement, the monoclinic Na_1VO_3 compound [51] has been reported to exhibit a voltage of ~5 V [52]. However, poor electrical conductivity limited its capacity to 50 $mAhg^{-1}$. Similar to our results for $\bar{3}$ Na_1VO_3, in the monoclinic polymorph, the redox reaction is dominantly carried out on O centers as V has a d^0 configuration in both compounds. We nonetheless predict that the desodiated $P\bar{3}1m$ $Na_{0.5}VO_3$ is metallic, as shown in Fig. 2(a). Consequently, $R\bar{3}$ structures, in principle, could be operated near the maximum theoretical capacity of 220 $mAhg^{-1}$. In addition to high voltage, $R\bar{3}$ Na_1VO_3 also enjoys robust stability against all major competing $Na_xV_yO_z$ phases. The stability of Na_1VO_3 against Na_1VO_2, in particular, is driven by the fact that the t_{2g} electrons of the V^{3+} ion in Na_1VO_2, due to trigonal distortion, adopt the antibonding e_g^* character [53]. Therefore, the loss of these electrons in Na_1VO_3 results in the stability of $R\bar{3}$ phase.

IV. CONCLUSIONS

Unhybridized oxygen states in $R\bar{3}$ (ilmenite structure) Na_1MO_3 compounds are the primary charge compensator during the redox reaction accompanied Na extraction/insertion for M = V, Cr, Mn, Fe, Co, Ni. Since the potential associated with O redox is higher than that of M redox, the proposed mechanism promises a new opportunity for designing high-voltage cathodes for Na battery applications. The most notable prediction is Na_1VO_3, which has a potential of 5.907 V and is thermodynamically stable with respect to major competing $Na_xV_yO_z$ compounds, as shown in Table S3–S5 in the Supplemental Material. Moreover, in all compounds, the bonding interaction between neighboring O pairs is rather weak, and the O–O distance remains relatively large at ~2.3 Å throughout cycling. However, in all compounds but Na_1VO_3, the O_2 evolution is still driven by a thermodynamic reduction of M to a lower oxidation state. The primary challenge in advancing this new paradigm in cathode design is, therefore, stabilizing the promising compounds with earth-abundant elements Na_1FeO_3 and Na_1MnO_3 that are predicted to have a potential of 5.178 and 4.530 V, respectively.

ACKNOWLEDGMENTS

This work was supported in part by the Ministry of Education, Culture, Sports, Science and Technology (MEXT), Japan; KAKENHI Grants No. JP15H05701 and No. JP19H05815, and "Priority Issue (No. 5) on Post K computer" (Development of new fundamental technologies for high-efficiency energy creation, conversion/storage, and use). The calculations were carried out on the supercomputers in NIMS, The University of Tokyo and Kyushu University, and the HPCI systems through the HPCI System Research Projects (Project IDs: hp170122, hp170174, hp170169, and hp180091).

[1] X. Xiang, K. Zhang, and J. Chen, Adv. Mater. **27**, 5343 (2015).
[2] M. S. Islam and C. A. J. Fisher, Chem. Soc. Rev. **43**, 185 (2014).
[3] C. Liu, Z. G. Neale, and G. Cao, Mater. Today **19**, 109 (2016).
[4] J. Y. Hwang, S. T. Myung, and Y. K. Sun, Chem. Soc. Rev. **46**, 3529 (2017).
[5] K. Kubota and S. Komaba, J. Electrochem. Soc. **162**, A2538 (2015).
[6] P. K. Nayak, L. Yang, W. Brehm, and P. Adelhelm, Angew. Chem. Int. Ed. **57**, 102 (2018).
[7] J. W. Choi and D. Aurbach, Nat. Rev. Mater. **1**, 16013 (2016).
[8] Y. You and A. Manthiram, Adv. Energy Mater. **8**, 1701785 (2018).
[9] M. H. N. Assadi and Y. Shigeta, J. Power Sources **388**, 1 (2018).
[10] J. M. Tarascon, G. Vaughan, Y. Chabre, L. Seguin, M. Anne, P. Strobel, and G. Amatucci, J. Solid State Chem. **147**, 410 (1999).
[11] B. Mortemard de Boisse, G. Liu, J. Ma. S. Nishimura, S.-C. Chung, H. Kikuchi, Y. Harada, J. Kikkawa, Y. Kobayashi, M. Okubo, and A. Yamada, Nat. Commun. **7**, 11397 (2016).
[12] M. H. N. Assadi, M. Okubo, A. Yamada, and Y. Tateyama, J. Mater. Chem. A **6**, 3747 (2018).
[13] R. Liu, G. Xu, Q. Li, S. Zheng, G. Zheng, Z. Gong, Y. Li, E. Kruskop, R. Fu, Z. Chen, K. Amine, and Y. Yang, ACS Appl. Mater. Interfaces **9**, 43632 (2017).
[14] L. Deng, X. Niu, G. Ma, Z. Yang, L. Zeng, Y. Zhu, and L. Guo, Adv. Funct. Mater. **28**, 1800670 (2018).
[15] K. Kawai, W. Zhao, S.-i. Nishimura, and A. Yamada, ACS Appl. Energy Mater. **1**, 928 (2018).
[16] K. Kubobuchi, M. Mogi, H. Ikeno, I. Tanaka, H. Imai, and T. Mizoguchi, Appl. Phys. Lett. **104**, 053906 (2014).
[17] H. Guo, Y. Hosaka, F. D. Romero, T. Saito, N. Ichikawa, and Y. Shimakawa, Inorg. Chem. **56**, 3695 (2017).
[18] R. Rajagopalan, B. Chen, Z. Zhang, X.-L. Wu, Y. Huang, B. Li, Y Zong, J. Wang, G.-H. Nam, M. Sindoro, S.-X. Dou, H.-K. Liu, and H. Zhang, Adv. Mater. **29**, 1605694 (2017).
[19] A. Grimaud, W. T. Hong, Y. Shao-Horn, and J. M. Tarascon, Nat. Mater. **15**, 121 (2016).
[20] G. Kresse and D. Joubert, Phys. Rev. B **59**, 1758 (1999).
[21] G. Kresse and J. Furthmüller, Phys. Rev. B **54**, 11169 (1996).
[22] G. Kresse and J. Furthmüller, Comput. Mater. Sci. **6**, 15 (1996).
[23] S. Maintz, V. L. Deringer, A. L. Tchougréeff, and R. Dronskowski, J. Comput. Chem. **37**, 1030 (2016).

[24] J. Heyd, G. E. Scuseria, and M. Ernzerhof, J. Chem. Phys. **118**, 8207 (2003).
[25] J. Heyd, G. E. Scuseria, and M. Ernzerhof, J. Chem. Phys. **124**, 219906 (2006).
[26] A. D. Becke and K. E. Edgecombe, J. Chem. Phys. **92**, 5397 (1990).
[27] A. Savin, B. Silvi, and F. Colonna, Can. J. Chem. **74**, 1088 (1996).
[28] See Supplemental Material at http://link.aps.org/supplemental/10.1103/PhysRevMaterials.4.015401 for additional information on the calculation details, details of the optimized structures, the stability, and the analysis of desodiation processes.
[29] R. Dronskowski and P. E. Bloechl, J. Phys. Chem. **97**, 8617 (1993).
[30] M. K. Aydinol, A. F. Kohan, G. Ceder, K. Cho, and J. Joannopoulos, Phys. Rev. B **56**, 1354 (1997).
[31] H. Li, Z. Wang, L. Chen, and X. Huang, Adv. Mater. **21**, 4593 (2009).
[32] W. Kobayashi and Y. Moritomo, J. Phys. Soc. Jpn. **83**, 104712 (2014).
[33] M. H. Han, E. Gonzalo, G. Singh, and T. Rojo, Energy Environ. Sci. **8**, 81 (2015).
[34] T. Shibata, Y. Fukuzumi, W. Kobayashi, and Y. Moritomo, Sci. Rep. **5**, 9006 (2015).
[35] C. Didier, M. Guignard, C. Denage, O. Szajwaj, S. Ito, I. Saadoune, J. Darriet, and C. Delmas, Electrochem. Solid-State Lett. **14**, A75 (2011).
[36] N. Yabuuchi, H. Yoshida, and S. Komaba, Electrochemistry **80**, 716 (2012).
[37] J. Zhao, L. Zhao, N. Dimov, S. Okada, and T. Nishida, J. Electrochem. Soc. **160**, A3077 (2013).
[38] N. Yabuuchi, M. Takeuchi, M. Nakayama, H. Shiiba, M. Ogawa, K. Nakayama, T. Ohta, D. Endo, T. Ozaki, T. Inamasu, K. Sato, and S. Komaba, Proc. Natl. Acad. Sci. (U.S.A.) **112**, 7650 (2015).
[39] A. Gutierrez, N. A. Benedek, and A. Manthiram, Chem. Mater. **25**, 4010 (2013).
[40] B. A. Wechsler and C. T. Prewitt, Am. Mineral. **69**, 176 (1984).
[41] M. Saubanere, E. McCalla, J. M. Tarascon, and M. L. Doublet, Energy Environ. Sci. **9**, 984 (2016).
[42] Y. Xie, M. Saubanere, and M. L. Doublet, Energy Environ. Sci. **10**, 266 (2017).
[43] M. Sathiya, G. Rousse, K. Ramesha, C. P. Laisa, H. Vezin, M. T. Sourgrati, M.-L. Doublet, D. Foix, D. Gonbeau, W. Walker, A. S. Prakash, M. B. Hassine, L. Dupont, and J.-M. Tarascon, Nat. Mater. **12**, 827 (2013).
[44] D. A. Kitchaev, Z. Lun, W. D. Richards, H. Ji, R. J. Clément, M. Balasubramanian, D.-H. Kwon, K. Dai, J. K. Papp, T. Lei, B. D. McCloskey, W. Yang, J. Lee, and G. Ceder, Energy Environ. Sci. **11**, 2159 (2018).
[45] C. Delmas, S. Brèthes, and M. Ménétrier, J. Power Sources **34**, 113 (1991).
[46] R. Wang, X. Li, L. Liu, J. Lee, D.-H. Seo, S.-H. Bo, A. Urban, and G. Ceder, Electrochem. Commun. **60**, 70 (2015).
[47] N. Twu, M. Metzger, M. Balasubramanian, C. Marino, X. Li, H. Chen, H. Gasteiger, and G. Ceder, Chem. Mater. **29**, 2584 (2017).
[48] J. Lee, A. Urban, X. Li, D. Su, G. Hautier, and G. Ceder, Science **343**, 519 (2014).
[49] D. H. Seo, J. Lee, A. Urban, R. Malik, S. Kang, and G. Ceder, Nat. Chem. **8**, 692 (2016).
[50] A. J. Perez, D. Batuk, M. Saubanère, G. Rousse, D. Foix, E. McCalla, E. J. Berg, R. Dugas, K. H. W. van den Bos, M.-L. Doublet, D. Gonbeau, A. M. Abakumov, G. Van Tendeloo, and J.-M. Tarascon, Chem. Mater. **28**, 8278 (2016).
[51] K. Li, L. Cao, Z. Huang, L. Chen, Z. Chen, and C. Fu, J. Power Sources **344**, 25 (2017).
[52] J. Zhang, B. Su, A. Kitajou, M. Fujita, Y. Cui, M. Oda, W. Zhou, P. H. L. Sit, and D. Y. W. Yu, J. Power Sources **400**, 377 (2018).
[53] M. H. N. Assadi and Y. Shigeta, RSC Adv. **8**, 13842 (2018).

Supplementary Information
Possible high potential ilmenite type Na_1MO_3 (M = V–Ni) cathodes realized by dominant oxygen redox reaction

M. Hussein N. Assadi,[1] Masashi Okubo,[2,3] Atsuo Yamada,[2,3] Yoshitaka Tateyama[1,3,*]

[1]*Center for Green Research on Energy and Environmental Materials (GREEN), International Center for Materials Nanoarchitectonics (MANA) and Center for Materials Research by Information Integration (CMI2), National Institute for Materials Science (NIMS), 1-1 Namiki, Tsukuba, Ibaraki 305-0044, Japan.*

[2]*Department of Chemical System Engineering, The University of Tokyo, 7-3-1 Hongo, Bunkyo-ku, Tokyo 113-8656, Japan.*

[3]*Elements Strategy Initiative for Catalysts & Batteries (ESICB), Kyoto University, 1-30 Goryo-Ohara, Nishikyo-ku, Kyoto 615-8245, Japan.*

I. CHOICE OF FUNCTIONAL

The generalized gradient approximation (GGA) of the exchange-correlation functional, which is most commonly used, often overly delocalizes the 3d electrons and underestimates the bandgap in transition metal oxides. These shortcomings lead to an inaccurate description of band alignment, which may distort the true picture of the redox mechanism. Consequently, corrections to the GGA method, such as the addition of an *ad hoc* Hubbard term (U_{eff}) or mixing with Hartree-Fock (hybrid), are commonly applied. In Figure S1, we present the partial density of states of Na_1FeO_3 compound calculated with hybrid functional HSE06 with a mixing parameter of 0.2 and various values of U_{eff} to compare the performance of these correction methods.

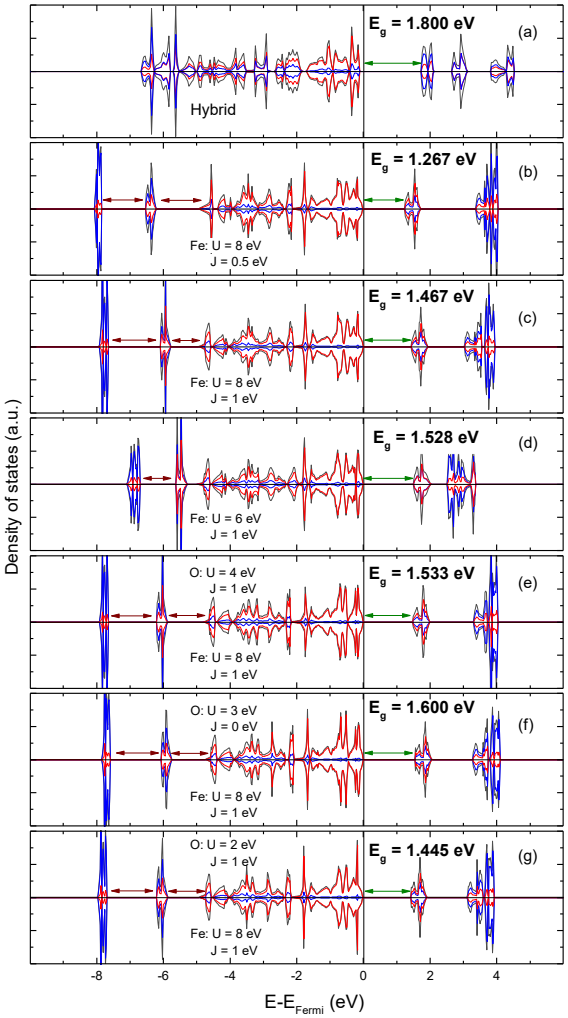

Figure S1. The partial density of states in the Na_1FeO_3 compound calculated with different functionals. The blue and red lines correspond to the 3d states of a single Fe ion and the 2p states of 6 coordinating O ions, respectively.

The band-gap produced by the hybrid method is 1.800 eV. The closest bandgap produced by GGA+U method was 1.600 eV using the following values $U = 8$ eV, $J = 1$ for Fe and $U = 3$ eV and $J = 1$ eV for O. However, the GGA+U method at these relatively large U_{eff} values gives an unphysical band description as it produces two pseudo-gaps in the valence band which are marked with brown double-arrows in Figure S1. Choosing smaller U_{eff} values eliminates the pseudo-gaps, but it also reduces the fundamental bandgap. Consequently, no acceptable compromise could be achieved using the GGA+U method that may produce a continuous valence band and sufficiently large band-gap. Therefore, the use of the hybrid functional is necessary for this class of materials for obtaining a realistic redox mechanism.

II. STRUCTURAL DETAILS OF $R\bar{3}$ Na_1MO_3 COMPOUNDS

Table S1 shows the lattice parameters of the ilmenite type $R\bar{3}$ $NaMO_3$ compounds. The hexagonal representation is the conventional representation, while the rhombohedral presentation constitutes the irreducible primitive representation. Both of these lattice structures belong to the trigonal crystal system and have the following relationship:

$$a_{Rhom} = \frac{a_{Hex}\beta}{3}, \text{ and } \alpha_{Rhom} = 2\sin^{-1}\frac{3\beta}{2} \text{ whereas } \beta := \sqrt{3 + \left(\frac{c_{Hex}}{a_{Hex}}\right)^2}. \quad \text{Equation S1}$$

Table S1. The calculated lattice parameters of the $R\bar{3}$ lattice structure in both hexagonal and rhombohedral representations.

System	a_{Hex} (Å) Hexagonal	c_{Hex} (Å) Hexagonal	a_{Rhom} (Å) Rhombohedral	α_{Rhom} (°) Rhombohedral
$NaVO_3$	5.003	15.225	5.840	50.729
$NaCrO_3$	4.988	15.166	5.818	50.769
$NaMnO_3$	4.917	15.425	5.873	49.489
$NaFeO_3$	4.913	15.341	5.848	49.681
$NaCoO_3$	4.885	15.317	5.833	49.516
$NaNiO_3$	4.858	15.667	5.928	48.378

III. STRUCTURAL DETAILS OF $P\bar{3}1m$ $Na_{0.5}MO_3$ COMPOUNDS

Table S2 shows the lattice parameters of the desodiated $P\bar{3}1m$ $Na_{0.5}MO_3$ compounds. The choice of $P\bar{3}1m$ structure for the desodiated compounds was inspired by the experimental observation of the desodiation of Na_1RuO_3 to $P\bar{3}1m$ $Na_{0.5}RuO_3$. The $P\bar{3}1m$ lattice (space group 162), similar to the sodiated $R\bar{3}$ lattice, belongs to the symmorphic trigonal crystal family.

Table S2. The lattice parameters of hexagonal $P\bar{3}1m$ $Na_{0.5}MO_3$ compounds.

System	a (Å) Hexagonal	c (Å) Hexagonal
$Na_{0.5}VO_3$	4.933	4.715
$Na_{0.5}CrO_3$	4.862	4.860
$Na_{0.5}MnO_3$	4.860	4.938
$Na_{0.5}FeO_3$	4.761	5.052
$Na_{0.5}CoO_3$	4.733	5.055
$Na_{0.5}NiO_3$	4.820	4.937

IV. STABILITY TREND IN HEXAGONAL $R\bar{3}$ Na_1MO_3 COMPOUNDS

In this section, we conducted a preliminary stability check of the hypothetical $R\bar{3}$ Na_1MO_3 compounds presented in the main Article. We, first, compared the total energy of the hexagonal $R\bar{3}$ Na_1MO_3 compounds with the total energy of cubic $Pm\bar{3}m$ Na_1MO_3 compounds ($SrTiO_3$ structure) using GGA+U methods. The U_{eff} value was set to 5 eV for all compounds and M ions. The calculations of the cubic structure were carried out using a 2 × 2 × 2 supercell with all internal coordinates and lattice parameters relaxed to accommodate any possible tilting and distortion. This comparison shows which polymorph is more stable upon synthesis under equilibrium conditions. Additionally, we considered different spin alignments that usually prevail in layered structures, *i.e.*, ferromagnetism, A-type antiferromagnetism, and G-type antiferromagnetism. In ferromagnetic state all, M ions have parallel spin direction. In A-type antiferromagnetic state, M ions within a plane are aligned ferromagnetically while the M ions across different planes are aligned antiferromagnetically. In the G-type antiferromagnetic state, M ions across the planes and within the planes are aligned

antiferromagnetically. The schematic representations of the lattice structures along with the spin direction of the *M* ions are given in Figure S2, while the relative total energies are given in Table S3. We found that non-magnetic $R\bar{3}$ Na_1VO_3, ferromagnetic $R\bar{3}$ Na_1CrO_3, Na_1MnO_3 and G-type antiferromagnetic $R\bar{3}$ Na_1FeO_3 and Na_1CoO_3 were more stable than their cubic counterparts. Na_1NiO_3, on the other hand, found to be more stable in ferromagnetic cubic $Pm\bar{3}m$ phase.

Table S3. The relative total energy of the Na_1MO_3 compounds per unit formula in meV for different spin alignments in both hexagonal and cubic structures is presented. The total energies of every compound are presented with respect to the most stable structure. As a result, zero energy in every column indicated the most stable structure.

System	$NaVO_3$	$NaCrO_3$	$NaMnO_3$	$NaFeO_3$	$NaCoO_3$	$NaNiO_3$
$R\bar{3}$ (FM)	0.000	0.000	0.000	58.096	65.308	356.803
$R\bar{3}$ (GAFM)		53.168	100.615	0.000	0.000	0.433
$R\bar{3}$ (AAFM)		3.016	6.492	58.391	64.584	0.370
$Pm\bar{3}m$ (FM)	21.411	349.735	553.519	653.624	704.846	0.000
$Pm\bar{3}m$ (GAFM)		353.699	541.063	874.646	124.141	0.070
$Pm\bar{3}m$ (AAFM)		406.499	601.544	732.961	688.037	0.441

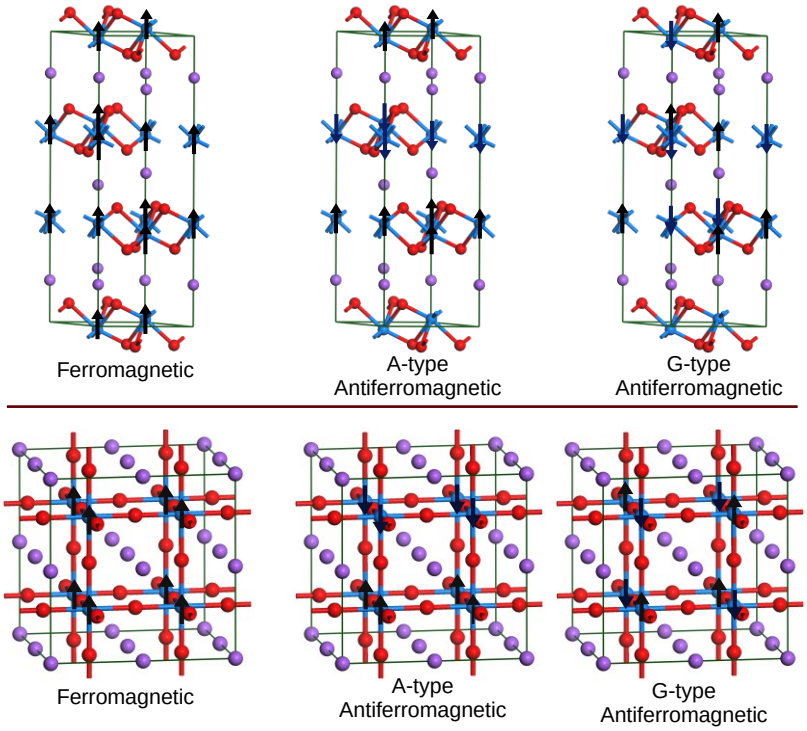

Figure S2. Schematic presentations of various spin alignments achievable in $R\bar{3}$ hexagonal (upper row) and cubic $Pm\bar{3}m$ (lower row) structures of Na_1MO_3 stoichiometry. The arrows indicate the spin direction of a given *M* ion. Red, blue, and purple spheres correspond to O, *M*, and Na ions, respectively.

Interestingly, the magnetic stability of the ilmenite type $R\bar{3}$ Na_1MO_3 compounds calculated with GGA+U functional, as presented in Table S3, exhibits the same trend as the HSE06 hybrid calculations presented in Table 1. However, the margin of stability varies depending on the choice of functional.

We, then, calculated the enthalpy of the reduction ($\Delta E_{Reduction}$) of $R\bar{3}$ Na_1MO_3 phase into $R\bar{3}m$ Na_1MO_2 phase using Eq. S2:

$$\Delta E_{Reduction} = E^{total}(Na_1MO_3) - E^{total}(Na_1MO_2) - \frac{1}{2}E^{total}(O_2) \qquad \text{Equation S2.}$$

Here E^{total} is the total density functional energy per unit formula. The results are presented in Table S4. Negative values indicate the stability of Na_1MO_3 against the Na_1MO_2 phase. According to Table S4, only Na_1VO_3 is readily stable against the competing Na_1VO_2.

Table S4. $\Delta E_{\text{Reduction}}$ values, as defined in Eq. S1.

	$NaVO_3$	$NaCrO_3$	$NaMnO_3$	$NaFeO_3$	$NaCoO_3$	$NaNiO_3$
$\Delta E_{\text{Reduction}}$ (eV)	−1.757	1.004	0.349	0.404	0.374	1.030

V. STABILITY OF $R\bar{3}$ Na_1VO_3 AGAINST COMPETING TERNARY PHASES

In the last section, we showed that $R\bar{3}$ Na_1VO_3 exhibits promising stability trends being more stable than both $Pm\bar{3}m$ $NaVO_3$ and $R\bar{3}$m $NaVO_2$. For further inquiry, we, here, examine the stability of $R\bar{3}$ Na_1VO_3 against major known compounds of $Na_xV_yO_z$ composition. In doing so, we calculated the decomposition enthalpy (ΔH) of $R\bar{3}$ Na_1VO_3 with respect to the identified most competitive combination (x,y,z) according to

$$\Delta H = nE^{total}(\mathrm{Na_1VO_3}) - 1E^{total}\left(\mathrm{Na_xV_yO_z}\right) - aE^{total}(\mathrm{V_2O_5}) - bE^{total}(\mathrm{Na_2O}) - cE^{total}(\mathrm{O_2}) \quad \text{Equation S3.}$$

where E^{total} is the total DFT energy of a given compound, and the constants n, a, b, c are chosen in a manner that maintain the mass balance under the constraint a, b, $c > 0$. Negative ΔH means that the $R\bar{3}$ Na_1VO_3 is more stable than a given competing $Na_xV_yO_z$ phase under the O-rich environment, and as such, it would not experience decomposition to that particular $Na_xV_yO_z$ phase. The competing ternary $Na_xV_yO_z$ were chosen by screening Materials Projects' (materialsproject.org) database. We only chose the most stable $Na_xV_yO_z$ structures. The calculated ΔH values are reported in Table S5 and indicate that $R\bar{3}$ Na_1VO_3 is stable against all considered competing phases.

Table S5. The decomposition enthalpy of $R\bar{3}$ V_1NaO_3 against the competing ternary (Na, V, O) phases. In the decomposition column, the left-hand side always denotes $R\bar{3}$ Na_1VO_3.

Competing ternary phase	Symmetry group	Materials Project identifier	Decomposition	Decomposition enthalpy, ΔH (eV)
$Na_2V_3O_7$	$P31c$	555416	$3\mathrm{NaVO_3} \rightarrow 1\mathrm{Na_2V_3O_7} + \frac{1}{2}\mathrm{Na_2O} + \frac{3}{4}\mathrm{O_2}$.	−1.809
$Na_2V_3O_7$	$P\bar{3}$	567133	$3\mathrm{NaVO_3} \rightarrow 1\mathrm{Na_2V_3O_7} + \frac{1}{2}\mathrm{Na_2O} + \frac{3}{4}\mathrm{O_2}$.	−1.789
Na_3VO_4	$Pmn2(1)$	780545	$3\mathrm{NaVO_3} \rightarrow 1\mathrm{Na_3VO_4} + 1\mathrm{V_2O_5}$.	−1.185
$Na_4V_2O_7$	$C2/c$	648893	$4\mathrm{NaVO_3} \rightarrow 1\mathrm{Na_4V_2O_7} + 1\mathrm{V_2O_5}$.	−1.187
Na_4VO_4	$P\bar{1}$	849942	$4\mathrm{NaVO_3} \rightarrow 1\mathrm{Na_4VO_4} + \frac{3}{2}\mathrm{V_2O_5} + \frac{1}{4}\mathrm{O_2}$.	−4.189
$Na_5V_{12}O_{32}$	Cm	765664	$12\mathrm{NaVO_3} \rightarrow 1\mathrm{Na_5V_{12}O_{32}} + \frac{7}{2}\mathrm{Na_2O} + \frac{1}{4}\mathrm{O_2}$.	−10.009
Na_5VO_5	$Pbcm$	25160	$5\mathrm{NaVO_3} \rightarrow 1\mathrm{Na_5VO_{5+}}2\mathrm{V_2O_5}$.	−4.704
$Na_9V_{14}O_{35}$	$P2/c$	578824	$14\mathrm{NaVO_3} \rightarrow 1\mathrm{Na_9V_{14}O_{35}} + \frac{5}{2}\mathrm{Na_2O} + \frac{9}{4}\mathrm{O_2}$.	−7.714
NaV_2O_5	$Pmn2(1)$	505821	$2\mathrm{NaVO_3} \rightarrow 1\mathrm{NaV_2O_5} + \frac{1}{2}\mathrm{Na_2O} + \frac{1}{4}\mathrm{O_2}$.	−1.424
NaV_2O_5	$Pnma$	765850	$2\mathrm{NaVO_3} \rightarrow 1\mathrm{NaV_2O_5} + \frac{1}{2}\mathrm{Na_2O} + \frac{1}{4}\mathrm{O_2}$.	−2.010
NaV_3O_8	$P2(1)/m$	764206	$3\mathrm{NaVO_3} \rightarrow 1\mathrm{NaV_3O_8}{+}1\mathrm{Na_2O}$.	−2.868
$NaVO_2$	$R\bar{3}m$	19391	$1\mathrm{NaVO_3} \rightarrow \mathrm{NaVO_{2+}}\frac{1}{4}\mathrm{O_2}$.	−1.757
$NaVO_3$	$C2/c$	19083	$1\mathrm{NaVO_3} \rightarrow \mathrm{NaVO_3}.(C2/c)$	−0.074
$NaVO_3$	$Pnma$	567447	$1\mathrm{NaVO_3} \rightarrow \mathrm{NaVO_3}.(Pnma)$	−0.360

VI. DESODIATION PROCESS

Table S6 shows the O–M–O bond angle and the shortest O–O distance (marked in Figure 1) for both sodiated Na_1MO_3 and desodiated $Na_{0.5}MO_3$ compounds. The change in the O–O shortest distance is quite small. It even slightly increases in Na_xCrO_3, Na_xFeO_3, and Na_xCoO_3. The magnitude of shortest O–O distance, therefore, on its own does not infer possible O_2 evolution during the desodiation process. Furthermore, there is no clear correlation between the cathode voltage and the shortest O–O distance or O–M–O bond angle.

The electronic localization function (ELF) iso-surface drawn at the ELF_{Max} values for each given compound is presented in Figure S3. Large ELF values (~1 - ~0.65) with the iso-surface basins localized around individual ions indicate ionic bonding. On the other hand, iso-surfaces that lie on the bond, between the atoms that are close to mid-point of the bond, indicate covalent bonding. We could not detect any ELF peaking at the bonds for any given compound. This demonstrates that all compounds had an ionic character. However, the degree of ionicity differed from compound to compound. Less ionic compounds such as Na_1VO_3 had a relatively smaller ELF_{Max} value and the ELF basins around O ions that were more spatially spread.

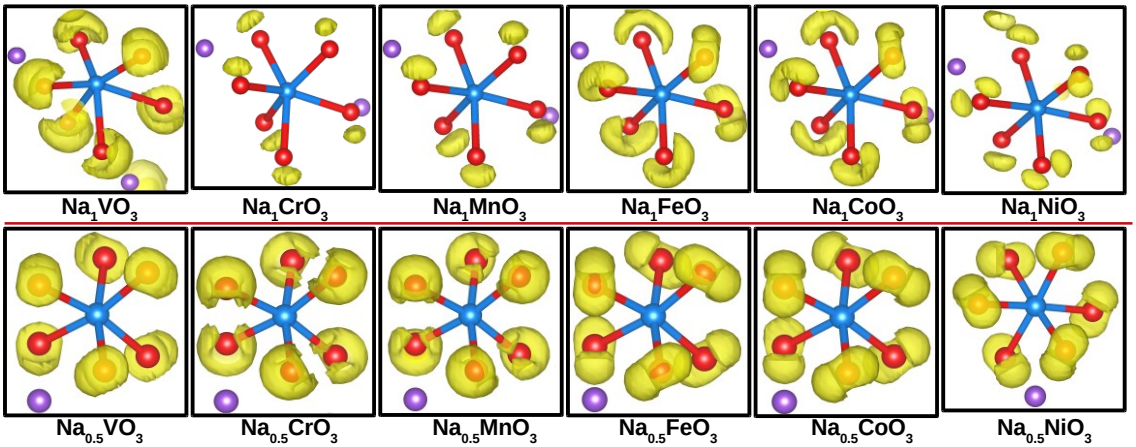

Figure S3. Iso-surfaces are corresponding the maximum values of the electronic localization (ELF_{Max}) function drawn for MO_6 octahedra. ELF_{Max} values are presented in Table 2 and Table 3

Table S6. The shortest O–O distance within a MO_6 octahedron, the O–M–O bond angle and the O–O distance across adjacent MO_6 octahedra along the c direction in both $R\bar{3}$ Na_1MO_3 and $P\bar{3}1m$ $Na_{0.5}MO_3$.

System	Shortest O–O distance (Å) Na_1MO_3	O–M–O angle Na_1MO_3	Cross octahedra O–O distance (Å) Na_1MO_3	Shortest O–O distance (Å) $Na_{0.5}MO_3$	O–M–O angle $Na_{0.5}MO_3$	Cross octahedra O–O distance (Å) $Na_{0.5}MO_3$
Na_xVO_3	2.401	102.612	3.321	2.368	100.514	2.951
Na_xCrO_3	2.283	91.802	3.228	2.342	100.322	3.860
Na_xMnO_3	2.347	92.986	3.395	2.427	98.276	3.143
Na_xFeO_3	2.324	93.947	3.416	2.381	98.204	3.213
Na_xCoO_3	2.291	92.259	3.382	2.368	98.148	3.300
Na_xNiO_3	2.401	93.724	3.535	2.386	98.785	3.426